Valley modulation and single-edge transport of magnons in breathing kagome ferromagnets

Yuheng Xing,[1,2] Hao Chen,[1] Ning Xu,[2] Xiao Li,[1,*] and Lifa Zhang[1,†]

[1]*NNU-SULI Thermal Energy Research Center (NSTER) and Center for Quantum Transport and Thermal Energy Science (CQTES), School of Physics and Technology, Nanjing Normal University, Nanjing 210023, China*

[2]*Deparment of Physics, Yancheng Institute of Technology, Yancheng 224051, China*

(Received 26 April 2021; revised 23 February 2022; accepted 25 February 2022; published 10 March 2022)

Owing to charge-free property, magnon is promising to achieve dissipationless transport without Joule heating. Valley degree of freedom has also been fully expressed in electronic structures, enabling information coding and manipulation via valley-based qubits. Considering the conceptual importance and application potential, it is highly desirable to couple valley to magnon excitation and realize their modulations. We demonstrate valley magnons and valley modulations in a kagome ferromagnetic lattice, with Dzyaloshinskii-Moriya and staggered exchange interactions. The staggered exchange interaction breaks spatial inversion symmetry, leading to magnon valley Hall effect. When the Dzyaloshinskii-Moriya interaction is further included, the valley degeneracy is lifted, exhibiting net anomalous Hall effect and a series of topological phase transitions. Single-edge heat transport of magnons can occur, with propagating currents along the edge and local circulating currents. These findings give full play to spin and valley degrees of freedom and add another dimension to magnonic device paradigms.

DOI: 10.1103/PhysRevB.105.104409

I. INTRODUCTION

With Dzyaloshinskii-Moriya interaction (DMI) that plays a role of vector potential like the Lorentz force [1,2], magnon Hall effect has been theoretically predicted and experimentally observed in magnetic insulators [3,4]. The magnon Hall systems, also named topological magnon insulator, are characterized by nonzero Chern numbers and topologically protected magnon edge states [5–15], similar to electronic topological insulators [16,17]. Quantum transport based on topological magnon edge states are highly promising to achieve dissipationless transport without Ohmic loss [18–24]. On the other hand, the valley degree of freedom has been fully expressed in electronic band structure of transition-metal dichalcogenides, where the valley carrier is selectively excited by chiral optical fields and measured by Berry-curvature-induced valley Hall current [25–28]. Valley degeneracy is also tunable by applied magnetic field or magnetic proximity effect [29]. Valleytronics, using valley degree of freedom as information carrier, has been a rising field in condensed matter physics. The explorations of both topological magnons and valleytronics have not only conceptual importance in basic quantum physics, but also application potential in advanced information technology [18,30].

Inequivalent energy valleys in magnon excitations, if they exist, are expected to directly inherit merits from both magnons and valleys, and possible modulations of valley magnons are likely to further give full play to spin and valley degrees of freedom. Compared with widely studied valley electrons, the studies of valley magnons have only a few examples, where the valley degeneracy is all kept [6,31–33]. There are attractive questions, e.g., whether the valley degeneracy of magnons is tunable like its electronic counterpart and correspondingly what transport behavior edge magnons will exhibit. Given that magnon Hall effect has been realized experimentally in pyrochlore structures with kagome layers [4,34] and valley physics is also present in the kagome lattice [31,35], we take a two-dimensional ferromagnetic kagome lattice as a prototype to investigate valley modulation and band topology in magnon excitation.

In this paper, the effects from staggered exchange interaction (SEI) [36], together with DMI, on valley magnons are taken into account. The SEI in neighboring triangles of the kagome lattice (see Fig. 1) creates gaps at $\pm K$ valleys and keeps valley degeneracy, similar to DMI. The combination of both interactions further lifts the valley degeneracy, and enables a transition from magnon valley Hall effect to net magnon anomalous Hall effect. The band exchange at valleys and associated topological phase transition also occur with varied interaction strengths. Further considering topological edge transport, besides the heat current flowing parallel to the edges, local circulating current appears within triangles of the kagome lattice. An asymmetric edge transport, mainly contributed by one edge, results from the valley splitting. These intriguing features realize modulations of the valley degeneracy, band topology, and associated edge transport in magnon excitation, which provides avenues for exploring energy-efficient device paradigms based on coupled spin and valley degrees of freedom.

II. MODELS AND METHODS

A. Calculations of the periodic monolayer

Figure 1(a) shows the pyrochlore structure formed by corner-sharing tetrahedra, which is the crystal structure

*lixiao@njnu.edu.cn
†phyzlf@njnu.edu.cn

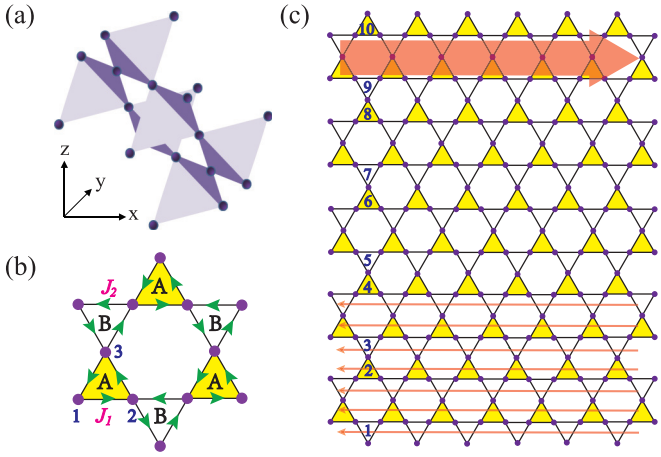

FIG. 1. Structures of the kagome lattice. (a) A pyrochlore structure including kagome layers. (b) A kagome lattice with staggered exchange interactions in neighboring A and B triangles. A unit cell includes three sites, denoted by 1–3. The arrows between nearest-neighboring sites denote the directions with DMI along $+z$. (c) A representative quasi-one-dimensional kagome strip, with ten triangles along its transversal direction.

of many magnon Hall ferromagnets, e.g., $In_2Mn_2O_7$ and $Ho_2V_2O_7$ [34]. Along the crystallographic [111] direction, there is a stacking of parallel kagome layers and intermediate triangular layers. Given that the kagome lattice supports both topological magnons and valley structure, we focus on valley magnons in a kagome monolayer. Taking into account SEI and DMI, a spin Hamiltonian of the lattice is given as [1,2,4,6,15,21,37–41]

$$\mathcal{H}=-J_1\sum_{\langle mn\rangle\in A}\boldsymbol{S}_m\cdot\boldsymbol{S}_n-J_2\sum_{\langle mn\rangle\in B}\boldsymbol{S}_m\cdot\boldsymbol{S}_n+D\sum_{\langle mn\rangle}\boldsymbol{\xi}_{mn}\cdot\boldsymbol{S}_m\times\boldsymbol{S}_n. \tag{1}$$

Here, $\boldsymbol{S}_{m,n}$ are spins on sites m,n, of which the nearest-neighboring interactions are considered. The first two terms describe exchange interactions in neighboring A and B triangles of the kagome lattice, respectively, as illustrated in Fig. 1(b), with $J_{1,2}$ being corresponding strengths. For $J_1=J_2$, the lattice has spatial inversion symmetry, while $J_1\neq J_2$ breaks the symmetry. Different $J_{1,2}$ can appear in a breathing kagome lattice with the A and B triangles having different sizes, which may result from additional layers adjacent to the kagome monolayer in real materials [36,42]. The third term denotes DMI with a strength of D. $\boldsymbol{\xi}_{mn}=+z/-z$ when the vector pointing from the nth site to the mth site is parallel/antiparallel to the arrow in Fig. 1(b).

Moreover, a more general lattice model has been constructed with both the exchange interaction and DMI being staggered in previous work [15], which discussed first- and second-order topological phases, but did not touch upon the valley properties and valley modulation in our study. We also consider the general lattice in our calculations. When taking into account that the staggered DMI is proportional to the SEI in the A and B triangles of the kagome lattice and the DMI is smaller than the exchange interaction, the conclusions on the valley splitting, band topology, and single-edge transport are qualitatively unchanged. Therefore, the simple model (1) gives robust results with a clear picture, which are shown in the main text. The results of the general model are provided in the Supplemental Material (SM hereafter) [43].

By the Holstein-Primakoff transformation [44,45] and the Fourier transformation, the magnon Hamiltonian in the momentum space of the model (1) reads

$$\mathcal{H}(\boldsymbol{k})=\begin{pmatrix}2(J_1+J_2)S & f_{12}(\boldsymbol{k}) & f_{31}^*(\boldsymbol{k})\\ f_{12}^*(\boldsymbol{k}) & 2(J_1+J_2)S & f_{23}(\boldsymbol{k})\\ f_{31}(\boldsymbol{k}) & f_{23}^*(\boldsymbol{k}) & 2(J_1+J_2)S\end{pmatrix}, \tag{2}$$

where $f_{\alpha\beta}(\boldsymbol{k})=\eta_1\exp(-i\phi_{\alpha\beta})+\eta_2\exp(i\phi_{\alpha\beta})$, with $(\alpha,\beta)=(1,2)$, $(2,3)$, and $(3,1)$. $\eta_{1,2}=-(J_{1,2}+iD)S$ and $\phi_{\alpha\beta}=\boldsymbol{k}\cdot(\boldsymbol{r}_\alpha-\boldsymbol{r}_\beta)$. $\boldsymbol{r}_\alpha$ is the coordinate of the αth site in a unit cell with $\alpha=1,2,3$ [Fig. 1(b)]. Without loss of generality, the spin magnitude, S, and J_1 are set to $\frac{1}{2}$ and the unit of the energy, respectively. J_2-J_1 and D are one order of magnitude smaller than J_1. Band structures and magnon properties, e.g., magnon Berry curvature, are computed by solving eigenstates of the Hamiltonian (2). More details of deriving the Hamiltonian and calculations can be found in the SM [43].

The momentum-resolved Berry curvature, $\Omega_l(\boldsymbol{k})$, of the lth magnon band is obtained by the relation

$$\Omega_l(\boldsymbol{k})=-2\hbar^2\mathrm{Im}\sum_{l'\neq l}\frac{\langle\psi_{l\boldsymbol{k}}|v_x|\psi_{l'\boldsymbol{k}}\rangle\langle\psi_{l'\boldsymbol{k}}|v_y|\psi_{l\boldsymbol{k}}\rangle}{(\epsilon_{l\boldsymbol{k}}-\epsilon_{l'\boldsymbol{k}})^2}, \tag{3}$$

where the magnon state is labeled by the band index l and the wave vector $\boldsymbol{k}$. $\epsilon_{l\boldsymbol{k}}$ and $\psi_{l\boldsymbol{k}}$ are the band energy and the wave function of the corresponding magnon state, respectively. The velocity operators, $v_x=\partial\mathcal{H}(\boldsymbol{k})/\hbar\partial k_x$ and $v_y=\partial\mathcal{H}(\boldsymbol{k})/\hbar\partial k_y$. The Chern number of the magnon band, as the integral quantity of $\Omega_l(\boldsymbol{k})$ over the entire Brillouin zone, is then given as [16,17,28,46]

$$\mathcal{C}_l=\frac{1}{2\pi}\int_{\mathrm{BZ}}dk_xdk_y\Omega_l(\boldsymbol{k}). \tag{4}$$

It is noted that the Berry curvature is well defined for the $\boldsymbol{k}$ point at which the band degeneracy is absent. As a result, the Chern number of one band is well defined for isolated bands.

B. Calculations of the nanostrip

To study topological heat transport of magnon edge states, a two-terminal device of a kagome strip is constructed. Left and right leads are added into two terminals of the central region. Three parts adopt the same kagome lattice. The corresponding magnon Hamiltonian of the two-terminal device in the momentum space has a form [6]

$$H=\begin{pmatrix}H_L & H_{LC} & 0\\ H_{CL} & H_C & H_{CR}\\ 0 & H_{RC} & H_R\end{pmatrix}, \tag{5}$$

Here, H_ζ with the subscript $\zeta=L,C,R$ are the components of the left lead, the central region, and the right lead, respectively. $H_{\zeta\zeta'}$ describes the coupling of corresponding parts. Based on these components, the Green's functions and self-energies are defined [6,47–50], and the definitions are given in the SM [43].

The heat transport of the two-terminal device is further calculated by a nonequilibrium Green's function method. The

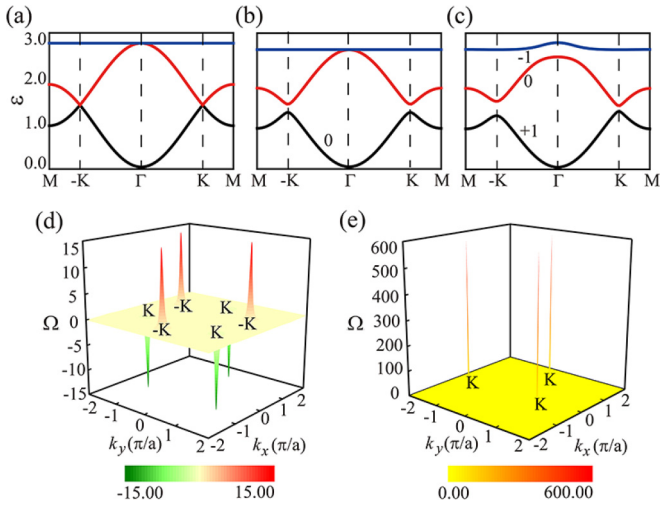

FIG. 2. Magnon dispersions and topological properties of kagome lattices. The band structures of the lattices (a) without SEI and DMI, (b) with SEI only, and (d) with both interactions. The parameters $(J_2, D) = (1.0, 0.0)$, $(0.9, 0.0)$, and $(0.9, 0.1)$ in (a)–(c), respectively, with $J_1 = 1.0$ being the unit of energy, where $J_{1(2)}$ and D are the strengths of the exchange interaction in the A (B) triangle and the DMI, respectively. The Chern number is labeled for each isolated band. (d),(e) The $\Omega(\boldsymbol{k})$ of the lowest band, using the parameters in (b) and (c), respectively.

local magnon density at the nth site for a certain band energy, ϵ, is obtained by the relation [6,51]

$$\rho_n(\epsilon) = \frac{i\hbar G^<_{nn}(\epsilon)}{\pi a}, \tag{6}$$

and the local magnon heat current from the nth site to its nearest-neighboring mth site is obtained by [6,52]

$$j_{mn}(\epsilon) = \frac{\epsilon}{2\pi}\mathrm{Re}[G^<_{mn}(\epsilon)H_{nm} - G^<_{nm}(\epsilon)H_{mn}], \tag{7}$$

where $G^<$ and a are the lesser Green's function and the lattice constant, respectively.

By summing over all the local currents in the interface, we then obtain the Landauer-like formula as

$$\langle J_L\rangle = \frac{1}{2\pi}\int_{-\infty}^{\infty}\epsilon[f_L(\epsilon) - f_R(\epsilon)]T(\epsilon)d\epsilon. \tag{8}$$

Here, $f_{L,R}(\epsilon) = 1/[\exp(\hbar\epsilon/k_BT_{L,R}) - 1]$ is the Bose-Einstein distribution function at the left/right lead, with $T_{L,R}$ being the temperature of the corresponding lead. $T(\epsilon)$ is the transmission coefficient and it is written as

$$T(\epsilon) = \mathrm{Tr}[G^r(\epsilon)\Gamma_L(\epsilon)G^a(\epsilon)\Gamma_R(\epsilon)], \tag{9}$$

where $G^r(\epsilon)$ and $G^a(\epsilon)$ are the retarded and advanced Green's functions, respectively. $\Gamma_{L,R}(\epsilon) = i[\Sigma^r_{L,R}(\epsilon) - \Sigma^a_{L,R}(\epsilon)]$ with $\Sigma^{r,a}(\epsilon)$ being corresponding self-energies.

III. RESULTS

A. Valleys in magnon excitations

Figures 2(a)– 2(c) show magnon band structures of the kagome lattices, where the bands of the lattice with uniform exchange interaction ($J_1 = J_2$) and vanishing DMI are taken as references. For this case, the topmost band is completely flat, which touches the middle band at the Brillouin zone center, Γ. The middle and lowest bands have Dirac-type dispersion in the vicinity of $\pm K$ points, i.e., vertices of the hexagonal Brillouin zone, and they touch at exactly $\pm K$, exhibiting degenerate, gapless valley structure. The entire magnon excitation is thus gapless as well.

With the SEI considered, band gaps open between the lower two bands at $\pm K$ valleys, while the flatness of the topmost band and the connection between the upper two bands at Γ are well kept, as shown in Fig. 2(b). This is in contrast to the case with nonvanishing DMI but uniform exchange interaction, where each band becomes isolated with band gap openings at both $\pm K$ and Γ, and the topmost band becomes uneven [31]. Moreover, when SEI or DMI is added, the valley degeneracy is still present, with equal band gaps at $\pm K$ valleys.

Further taking into account both interactions, besides isolated bands, the valley degeneracy is lifted, that is, magnon energies and band gaps at $\pm K$ become unequal in Fig. 2(c). The valley splitting offers an energy window for realizing valley-selective magnon excitation by a magnon waveguide. The valley index corresponding to a large (or small) band gap is determined by both signs of the DMI strength, D, and the relative magnitude of SEI. When the sign of $(J_1 - J_2)D$ is positive, small and large gaps are localized at K and $-K$ valleys, respectively. When the sign is negative, the relative gap sizes are interchanged.

The above evolution of the valleys at $\pm K$ can be well captured by an effective model. For the two lower bands, the effective model at $\pm K$ reads

$$\mathcal{H}_{\mathrm{eff}} = -\frac{\sqrt{3}(J_1+J_2)S}{4}\tau(q_x\sigma_x + q_y\sigma_y) + \left[\sqrt{3}D - \frac{3}{2}\tau(J_1 - J_2)\right]S\sigma_z, \tag{10}$$

where two parts of the model correspond to the pristine gapless Dirac state and the mass term that leads to band gap opening at $\pm K$ valleys, respectively, while an immaterial energy shift is ignored. $\boldsymbol{q}$ is the wave vector with respect to $\pm K$. $\sigma_{x,y,z}$ are Pauli matrices in the orbital space, and the valley index, $\tau = \pm 1$, denotes two valleys, respectively. The derivation of the model is provided in the SM [43]. According to the mass term with the mass $\Delta = [\sqrt{3}D - 3\tau(J_1 - J_2)/2]S$, a band gap of $2|\Delta|$ opens at the τK valley. It is seen that a nonzero band gap ($\Delta \neq 0$) requires nonvanishing SEI or DMI. With SEI or DMI, the band gaps at two valleys are equal. In contrast, both interactions lead to valley-dependent band gaps. The model clearly elucidates the band-gap variations in the numerical calculations. Moreover, the SEI gives rise to opposite masses at two valleys, while the DMI corresponds to the same mass. The sign variation of the mass indicates the change of the band ordering. The band topology and associated topological phase transition can be thus expected by introducing both interactions.

B. Band topology and topological phase transition

The momentum-resolved Berry curvature, $\Omega(\boldsymbol{k})$, and associated Chern number of magnon bands are further computed

as indicators of topological quantum transport. They are shown in Figs. 2(d) and 2(e) and labeled on each isolated band in Figs. 2(b) and 2(c), respectively. When both SEI and DMI are absent, $\Omega(\boldsymbol{k})$ is zero for each $\boldsymbol{k}$ point without band crossing. Therefore, there is no anomalous Hall transport induced by the Berry curvature.

When the SEI is added, $\Omega(\boldsymbol{k})$ becomes nonvanishing, and it has opposite extrema with the same magnitude at $\pm K$ valleys for the lower two bands. The Chern number, as the integral quantity of $\Omega(\boldsymbol{k})$, is thus zero for the isolated lowest band. Although the magnon band is topologically trivial, opposite $\Omega(K)$ and $\Omega(-K)$ endow valley magnons opposite anomalous velocities and consequently induce transversal Hall heat currents along opposite directions, under a longitudinal temperature gradient. It is a magnon version of the valley Hall effect. This is also different from the case with nonzero DMI, which has the same distribution of $\Omega(\boldsymbol{k})$ at $\pm K$ valleys, nonzero Chern numbers for magnon bands, and associated topological edge transport [6,31].

For a breathing lattice with nonzero DMI, $\Omega(\boldsymbol{k})$ at two valleys does not exhibit the same magnitude any longer, owing to the valley splitting. As a result, a net magnon anomalous Hall heat current is realized, no matter whether a single valley or both valleys are excited by the magnon waveguide, since anomalous Hall currents contributed by two valleys cannot completely cancel each other. This is in contrast to the lattice with only SEI where the net Hall current is absent. The net Hall heat current can be readily measured by induced transversal temperature difference, which is expected to be used as an information carrier in advanced device paradigms.

The distinct Berry curvatures above are associated with distinct massive terms of gapped Dirac states arising from SEI and DMI. Based on the above effective Dirac model (10) at $\pm K$ valleys, the Berry curvatures at two valleys are computed as

$$\Omega(\boldsymbol{q}) = \frac{t'^2\Delta}{2\left[t'^2\left(q_x^2+q_y^2\right)+\Delta^2\right]^{3/2}}, \tag{11}$$

where $t' = \sqrt{3}(J_1+J_2)S/4$ is the strength coefficient of the first term in the effective model, denoting the coupling interaction between orbitals. The sign of the Berry curvature is only determined by the sign of the mass Δ at each valley. The size of the Berry curvature at $\pm K$ is inversely proportional to Δ^2. Therefore, the variations of the Berry curvatures at two valleys are mainly attributed to the changes of the masses. It is well understood that while single DMI or SEI leads to the same magnitudes of the band gaps and associated Berry curvatures at two valleys, the Berry curvature is larger for the valley with a smaller band gap for the case with both interactions considered.

Moreover, topological phase transitions can occur, depending on interaction strengths. The interaction strengths $J_{1,2}$ and D are expected to be different in various magnetic materials and tunable by, e.g., applied strain or electric field for a certain material [53–57]. The topological phase diagrams of three magnon bands are shown in Figs. 3(a)– 3(c), respectively, as functions of J_2 and D. For the orange region in the figures, there are negative magnon excitation energies in the magnon spectrum of the ferromagnetic kagome lattice, indicating that

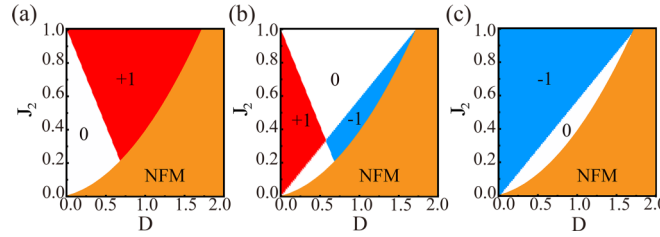

FIG. 3. The topological phase diagrams of three magnon bands, as functions of the strengths of D and J_2. (a), (b), and (c) correspond to the bottom, middle. and top bands, respectively. The Chern number of the magnon band is labeled in corresponding regions, except for the orange region that is nonferromagnetism (NFM).

the ferromagnetic order is unstable in the region. In addition, since the origin of the DMI is the spin-orbit interaction that is usually small compared with the exchange interaction, the relatively large D in the region is hard to realize in real materials. Therefore, the properties in the region are not discussed here [31,58,59]. For the other regions, the ferromagnetic order is stable and we thus compute the corresponding Chern number of magnon bands. In the ferromagnetic region, depending on strengths of SEI and DMI, the Chern number of the magnon band has a discrete number of -1, $+1$, or 0. A boundary between the regions with different Chern numbers corresponds to a vanishing band gap. When moving through the boundary, there is a topological phase transition with an exchange of the band ordering. In the process, the decrease, closure, and reopening of the band gap occur in turn. For the lower two bands, the band exchange appears at $\pm K$ valleys. In contrast, it appears at Γ for the upper two bands.

Specific to the isolated lowest band, the phase transition can be easily found from two limits. The lowest band has the Chern number of 0 and 1, with only SEI and only DMI considered, respectively. For an existing SEI, the Chern number changes from 0 to 1 as DMI is added and enhanced. Meanwhile, the band exchange appears at K, giving rise to varied Chern numbers, while the gap at $-K$ always increases without the band exchange. Therefore, the Chern number is determined by the relative magnitudes of SEI and DMI. Figure 2(c) corresponds to a relatively large DMI, and its bands have the same Chern numbers as the ones with only DMI.

C. Chiral magnon edge transport

Considering the above significant modifications of valley and topological properties in the kagome lattice, we further study magnon transport carried by the topological edge states. Given that the topological edge states are associated with nonzero Chern numbers according to bulk-edge correspondence, and the bands in Fig. 2(c) have nonzero Chern numbers, the edge transport in the lattice with both DMI and SEI is focused on. A nanostrip of the kagome lattice, similar to that in Fig. 1(c), is constructed with 40 triangles along its transversal direction and used in our calculation.

Figure 4(a) demonstrates the magnon band structure of the kagome strip with both interactions, where the choices of $J_{1,2}$ and D are the same as those in Fig. 2(c). Owing to the nontrivial band topology shown in Fig. 2(c), there are

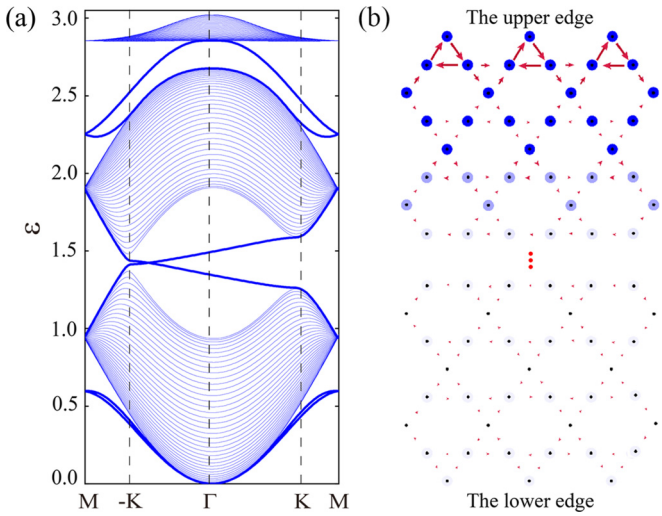

FIG. 4. Magnon properties of the kagome strip with both SEI and DMI. (a) The band structure of the strip. (b) Corresponding local heat current and local density in the strip. The arrow and circle denote the current and density, respectively, with the size and color saturation being proportional to respective magnitude.

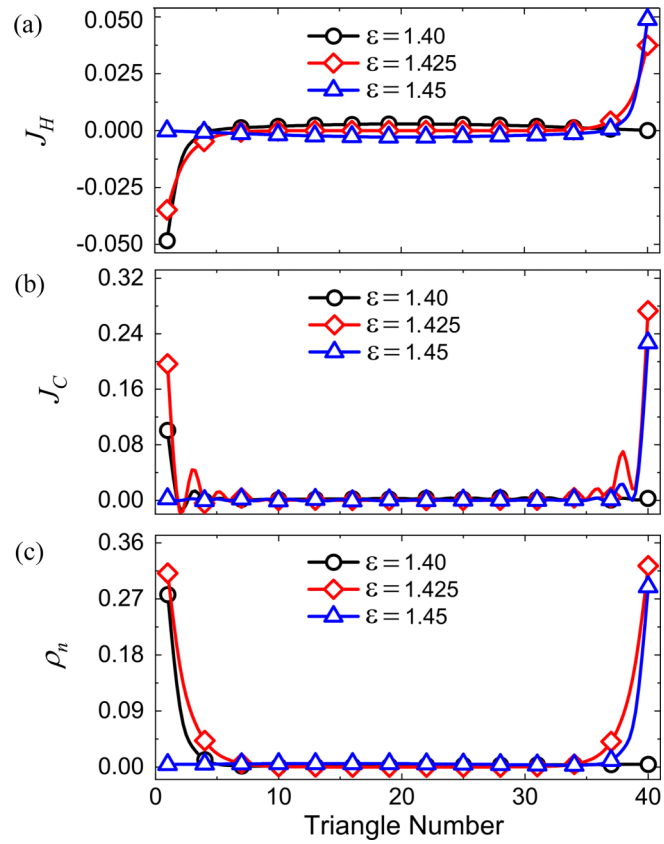

FIG. 5. The evolutions of local currents and density along the transversal direction of the strip. (a) Local horizontal current. (b) Local circulating current. (c) Local magnon density.

indeed topologically protected edge states within band gaps. The edge states within each gap are composed by one pair of gapless modes with opposite group velocities. For edge modes between the upper two bulk bands, the crossing point of the counterpropagating modes is located at the boundary of the one-dimensional Brillouin zone, M. As for the lower band gap, the edge modes connect $\pm K$ valleys. The crossing point of the edge modes is closer to the $-K$ valley, compared with the K valley, which is due to the valley splitting.

We then construct a two-terminal device of the kagome strip to investigate topological edge heat transport within the lower gap, using a nonequilibrium Green's function method [60]. Two semi-infinite leads are added at the left and right terminals of the strip, with temperatures of T_L and T_R, respectively. The transmission coefficient of the equilibrium edge transport is firstly calculated for the kagome strip. Since the transmission coefficient is determined by the number of propagating edge modes along a given longitudinal direction of the strip, it is always one within the band gap, independent of the temperature gradient.

In order to demonstrate spatial distribution of the edge transport, local heat current, $j_{mn}(\epsilon)$, from the site n to its nearest-neighboring site m and local magnon density, $\rho_n(\epsilon)$, at the site n are further computed for a given energy, ϵ. Here, equilibrium transport without the temperature gradient ($T_L = T_R$) is mainly considered, and nonequilibrium transport ($T_L \neq T_R$) will also be discussed later. The equilibrium distributions of local currents and densities are shown in Fig. 4(b). It is seen that circulating currents flow along three bonds of triangles in the kagome lattice. The magnitudes of j_{mn} along two oblique bonds are the same, but unequal to that along the horizontal bond. Therefore, a net forward or backward current along the horizontal bond, i.e., the edge direction of the strip, also exists, together with circulating current. For each triangle, the circulating current, j_C, and the net horizontal current, j_H, are defined as local current along the oblique bond and current difference between the horizontal and oblique bonds, respectively, with the direction from left to right being the positive direction. The heat currents, j_H and j_C, are shown in Fig. 5 for each triangle along the transversal direction of the strip, while the longitudinal direction keeps the translational symmetry. For the triangles with sizable local currents, both j_H and j_C are nonvanishing, and j_C is several times larger than j_H. The nonzero j_H is determined by the band topology and it takes responsibility for topological chiral edge transport, while nonzero j_C is a magnon characteristic of the kagome lattice with triangular fine structure. The circulating current, J_C, is the rotation along the triangular structure of the kagome lattice, different from the self-rotation motion of the magnon wave packet around its center due to the Berry phase effect [61,62].

Looking at evolutions of local densities and heat currents along the transversal direction of the strip, there are obvious asymmetric distributions between two edges when the magnon energy is close to the bulk band edge. For an energy $\epsilon = 1.45$, near the upper band, sizable currents and densities are well localized at the upper edge of the strip, while they disappear in the lower half of the strip, as demonstrated by the distributions in Fig. 4(b) and the blue curves in Fig. 5. Instead, a weak background j_H spreads transversely across the entire strip, and it is opposite to j_H at the upper edge [see Fig. 5(a)], ensuring that the total chiral current is zero at equilibrium. The asymmetric distribution exhibits characteristics

of single-edge transport. This is because the valley splitting makes two counterpropagating modes at the chosen energy have distinct energy differences with respect to bulk band and corresponding distinct spatial localizations. Moreover, when the chosen energy is near the lower bulk band ($\epsilon = 1.40$), the single-edge transport is shifted to the lower edge, with the horizontal currents flowing in the opposite direction. When the energy is close to the midgap ($\epsilon = 1.425$), edge modes are far away from bulk bands in energy and consequently localized at both edges with a weak asymmetry. The evolutions of $J_{H,C}$ and ρ_n at the outermost triangles of two edges with the varied energy are also given in the SM to further demonstrate frequency-tunable asymmetric transport [43]. In contrast, for varied energies within the band gap, the strip with only DMI always exhibits a topological edge transport with symmetric spatial distribution localized at two edges [6].

Moreover, the chiral edge transport is influenced by the signs of $(J_1 - J_2)$ and D, which is similar to the valley splitting of bulk band and shown in detail in the SM [43]. Opposite $J_1 - J_2$ leads to single-edge transports localized at opposite edges, with opposite current directions. The chirality of edge transport is thus invariant. In contrast, opposite D gives rise to a direction reversal of the current at the same edge, leading to edge transports with opposite chiralities. The change of the chirality results from the reversal of bulk Chern numbers by reversing D, while opposite $J_1 - J_2$ gives the same band topology and chirality.

IV. DISCUSSIONS

The above various Hall effects and the single-edge chiral transport in the kagome ferromagnet are expected to be detected experimentally, e.g., by spatial-resolved magnon temperature measurement [63] or magneto-optical Kerr effect [64], and they thus have potential use in information encoding and manipulation at the microscopic level. The study adds different dimensions to the exploration of unique device paradigms based on coupled spin and valley degrees of freedom.

Given that the asymmetric edge transport is obtained at equilibrium, we further computed topological edge transport with two leads at different temperatures, which may be another experimental available knob to tune the edge transport. Compared with the equilibrium transport, the nonequilibrium edge current, flowing from heat lead to cold lead, is enhanced, while the opposite current is weakened. As a result, a net heat current is generated and the asymmetric spatial distribution can be enhanced or weakened in the nonequilibrium edge transport.

The valley modulations and single-edge transport in magnon excitation are proposed in a ferromagnetic kagome lattice. These characteristics are expected to have generalizations to other crystal lattices (e.g., hexagonal lattice) and other magnetic orders (e.g., collinear and noncollinear antiferromagnetism) [9], which are worth further study. The first-principles calculations could also be performed in future work to further give quantitative parameters of realistic materials.

V. CONCLUSION

In summary, we studied valley magnons in a kagome lattice. Valley degeneracy and band topology are tunable by introducing SEI and DMI. As a result, both magnon valley Hall effect and topological edge transport are expected to be realized. Topological edge transport includes local circulating currents due to the fine triangular structure of the kagome lattice and propagating currents flowing along the edge direction. These currents can be localized at one edge to achieve single-edge transport by tuning valley splitting and frequency. The valley modulation of magnons and associated asymmetric transport provide new opportunities for designing energy-efficient spintronic and valleytronic devices.

ACKNOWLEDGMENTS

We thank Q. Niu and H. Jiang for helpful discussions. The work was supported by the National Natural Science Foundation of China (Grants No. 11890703, No. 11975125, and No. 11904173) and MOST (Grant No. 2017YFA0303500). X.L. is supported by the Jiangsu Specially-Appointed Professor Program. Y.X. is also supported by the Basic Science (Natural Science) Research Project of Higher Education Institutions in Jiangsu Province (Grant No. 21KJB140022).

[1] I. Dzyaloshinskii, J. Phys. Chem. Solids **4**, 241 (1958).
[2] T. Moriya, Phys. Rev. **120**, 91 (1960).
[3] H. Katsura, N. Nagaosa, and P. A. Lee, Phys. Rev. Lett. **104**, 066403 (2010).
[4] Y. Onose, T. Ideue, H. Katsura, Y. Shiomi, N. Nagaosa, and Y. Tokura, Science **329**, 297 (2010).
[5] K. A. van Hoogdalem, Y. Tserkovnyak, and D. Loss, Phys. Rev. B **87**, 024402 (2013).
[6] L. Zhang, J. Ren, J. S. Wang, and B. Li, Phys. Rev. B **87**, 144101 (2013).
[7] S. A. Owerre, Phys. Rev. B **94**, 094405 (2016).
[8] A. Mook, B. Gobel, J. Henk, and I. Mertig, Phys. Rev. B **95**, 020401(R) (2017).
[9] K. S. Kim, K. H. Lee, S. B. Chung, and J. G. Park, Phys. Rev. B **100**, 064412 (2019).
[10] W. Cai, J. Han, F. Mei, Y. Xu, Y. Ma, X. Li, H. Wang, Y. P. Song, Z. Y. Xue, Z. Q. Yin, S. Jia, and L. Sun, Phys. Rev. Lett. **123**, 080501 (2019).
[11] H. Zhang, X. Feng, T. Heitmann, A. I. Kolesnikov, M. B. Stone, Y. M. Lu, and X. Ke, Phys. Rev. B **101**, 100405(R) (2020).
[12] T. Hirosawa, S. A. Diaz, J. Klinovaja, and D. Loss, Phys. Rev. Lett. **125**, 207204 (2020).
[13] S. Park and B. J. Yang, Phys. Rev. B **102**, 214421 (2020).
[14] S. Park, N. Nagaosa, and B. Yang, Nano Lett. **20**, 2741 (2020).
[15] A. Sil and K. Ghost, J. Phys.: Condens. Matter **32**, 205601 (2020).

[16] M. Z. Hasan and C. L. Kane, Rev. Mod. Phys. **82**, 3045 (2010).
[17] X. L. Qi and S. C. Zhang, Rev. Mod. Phys. **83**, 1057 (2011).
[18] R. Shindou, R. Matsumoto, S. Murakami, and J. I. Ohe, Phys. Rev. B **87**, 174427 (2013).
[19] A. Mook, J. Henk, and I. Mertig, Phys. Rev. B **90**, 024412 (2014).
[20] M. Mena, R. S. Perry, T. G. Perring, M. D. Le, S. Guerrero, M. Storni, D. T. Adroja, Ch. Ruegg, and D. F. McMorrow, Phys. Rev. Lett. **113**, 047202 (2014).
[21] R. Chisnell, J. S. Helton, D. E. Freedman, D. K. Singh, R. I. Bewley, D. G. Nocera, and Y. S. Lee, Phys. Rev. Lett. **115**, 147201 (2015).
[22] S. A. Owerre, J. Phys. Commun. **1**, 025007 (2017).
[23] K. Nakata, S. K. Kim, J. Klinovaja, and D. Loss, Phys. Rev. B **96**, 224414 (2017).
[24] Y. M. Li, J. Xiao, and K. Chang, Nano Lett. **18**, 3032 (2018).
[25] D. Xiao, W. Yao, and Q. Niu, Phys. Rev. Lett. **99**, 236809 (2007).
[26] K. F. Mak, K. L. McGill, J. Park, and P. L. McEuen, Science **344**, 1489 (2014).
[27] J. Lee, K. F. Mak, and J. Shan, Nat. Nanotechnol. **11**, 421 (2016).
[28] Y. Xing, X. F. Xu, and L. Zhang, Acta Phys. Sin. **66**, 226601 (2017).
[29] J. Qi, X. Li, Q. Niu, and J. Feng, Phys. Rev. B **92**, 121403(R) (2015).
[30] V. V. Kruglyak, S. O. Demokritov, and D. Grundler, J. Phys. D: Appl. Phys. **43**, 264001 (2010).
[31] Y. Xing, F. Ma, L. Zhang, and Z. Zhang, Sci. China: Phys., Mech. Astron. **63**, 107511 (2020).
[32] R. Hidalgo-Sacoto, R. I. Gonzalez, E. E. Vogel, S. Allende, J. D. Mella, C. Cardenas, R. E. Troncoso, and F. Munoz, Phys. Rev. B **101**, 205425 (2020).
[33] X. Zhai and Y. M. Blanter, Phys. Rev. B **102**, 075407 (2020).
[34] T. Ideue, Y. Onose, H. Katsura, Y. Shiomi, S. Ishiwata, N. Nagaosa, and Y. Tokura, Phys. Rev. B **85**, 134411 (2012).
[35] N. Lera, D. Torrent, P. San-Jose, J. Christensen, and J. V. Alvarez, Phys. Rev. B **99**, 134102 (2019).
[36] P. Hogl, T. Frank, K. Zollner, D. Kochan, M. Gmitra, and J. Fabian, Phys. Rev. Lett. **124**, 136403 (2020).
[37] Y. Su, X. S. Wang, and X. R. Wang, Phys. Rev. B **95**, 224403 (2017).
[38] W. Heisenberg, Z. Phys. **49**, 619 (1928).
[39] I. Bose and U. Bhaumik, J. Phys.: Condens. Matter **6**, 10617 (1994).
[40] A. L. Chernyshev and P. A. Maksimov, Phys. Rev. Lett. **117**, 187203 (2016).
[41] A. Ruckriegel, A. Brataas, and R. A. Duine, Phys. Rev. B **97**, 081106 (2018).
[42] J. Yin, S. Zhang, G. Zhang *et al.*, Nat. Phys. **443**, 15 (2019).
[43] See Supplemental Material at http://link.aps.org/supplemental/10.1103/PhysRevB.105.104409 for calculation details, the energy dependence of topological edge transport, the effect from the sign changes of SEI and DMI, and the effect from the staggered DMIs.
[44] T. Holstein and H. Primakoff, Phys. Rev. **58**, 1098 (1940).
[45] L. Zhang, J. S. Wang, and B. Li, Phys. Rev. B **78**, 144416 (2008).
[46] D. Xiao, M. C. Chang, and Q. Niu, Rev. Mod. Phys. **82**, 1959 (2010).
[47] H. Haug and A. P. Jauho, *Quantum Kinetics in Transport and Optics of Semiconductors* (Springer, Berlin, 1996).
[48] J. S. Wang, J. Wang, and J. T. Lu, Eur. Phys. J. B **62**, 381 (2008).
[49] S. Doniach, and E. H. Sondheimer, *Green's Functions for Solid State Physicists* (W. A. Benjamin, 1974).
[50] G. D. Mahan, *Many Particle Physics*, 3rd ed. (Kluwer Academic, 2000).
[51] W. Zhang, T. S. Fisher, and N. Mingo, Numer. Heat Transfer, Part B **51**, 333 (2007).
[52] J. Li, T. C. A. Yeung, C. H. Kam, X. Zhao, Q. H. Chen, Y. Peng, and C. Q. Sun, J. Appl. Phys. **106**, 054312 (2009).
[53] S. Qi, J. Jiang, and W. Mi, Phys. Chem. Chem. Phys. **22**, 23597 (2020).
[54] C. Xu, Q. Wang, B. Xu, and J. Hu, Front. Phys. **16**, 53502 (2021).
[55] T. Liu and G. Vignale, Phys. Rev. Lett. **106**, 247203 (2011).
[56] S. Mankovsky, E. Simon, S. Polesya, A. Marmodoro, and H. Ebert, Phys. Rev. B **104**, 174443 (2021).
[57] C. Huang, L. Z. Jiang, Y. Zhu, Y. F. Pan, J. Y. Fan, C. L. Ma, J. Hu, and D. N. Shi, Phys. Chem. Chem. Phys. **23**, 22246 (2021).
[58] A. Mook, J. Henk, and I. Mertig, Phys. Rev. B **89**, 134409 (2014).
[59] K. Essafi, O. Benton, and L. D. C. Jaubert, Nat. Commun. **7**, 10297 (2016).
[60] H. Haug and A. P. Jauho, *Quantum Kinetics in Transport and Optics of Semiconductors* (Springer, Berlin, 1996).
[61] R. Matsumoto and S. Murakami, Phys. Rev. Lett. **106**, 197202 (2011).
[62] R. Matsumoto and S. Murakami, Phys. Rev. B **84**, 184406 (2011).
[63] M. Agrawal, V. I. Vasyuchka, A. A. Serga, A. D. Karenowska, G. A. Melkov, and B. Hillebrands, Phys. Rev. Lett. **111**, 107204 (2013).
[64] D. A. Allwood, G. Xiong, M. D. Cooke, and R. P. Cowburn, J. Phys. D: Appl. Phys. **36**, 2175 (2003).